FINAL YEAR PROJECT REPORT

_____

OPTIMISING THE LION BEAMLINE FOR THE ENERGY SELECTION OF LASER-ACCELERATED PROTONS

R. PULLAN

CID: 02020232

_____

A REPORT SUBMITTED IN PART FULFILMENT OF THE DEGREE OF

BACHELOR OF SCIENCE (HONS) IN PHYSICS

SUPERVISOR: PROF. KENNETH LONG

ASSESSOR: PROF. ALEXANDER TAPPER

DEPARTMENT OF PHYSICS

IMPERIAL COLLEGE LONDON

JANUARY 15, 2024

Abstract

This work presents an energy selection method for the LION beamline to maximise the delivery rate at a range of delivered proton energies. This method involved varying the position of two permanent magnet quadrupoles within the beamline to adjust the proton energy focused at the end of the beamline. Two functions are presented as the optimisation result, where a desired energy delivery is given as the input and the two quadrupole positions required to achieve this energy are calculated as the output. These optimal results were verified with a BDSIM model, where a strong agreement was found for the energy delivered at the optimised quadrupole positions. The optimisation method was conducted systematically so that the particle trajectory and RMS of the beam throughout the beamline can also be studied. These plots provided some insight into the relationship between quadrupole position and delivered energy. It was found a two peak delivered energy histogram is produced when a different energy is focused in each transverse plane in the beamline. To achieve a maximum delivery rate, the quadrupoles must be aligned with each other such that the same energy is focused in each transverse plane at the end of the beamline.

Declaration

This report has been prepared on the basis of my own work. Where other published and unpublished source materials have been used, these have been acknowledged. This work was not a group project. I have previously undertaken a summer UROP project with this supervisor, however the work presented here was undertaken after that project and is an independent study.

Word Count: 5807

Student Name: Riddhika Pullan

Date of Submission:15/01/24

Table of Contents

Chapter 1: **Introduction**

1.1 Particle Accelerators for Radiobiological Applications

Radiation therapy is an invaluable and effective tool in cancer treatment. It utilizes ionizing radiation to either kill or restrict the growth of tumour cells. Common treatment centres generally use high energy X-rays to kill tumour cells, however X-rays deposit energy as they travel so they can cause significant damage to the surrounding healthy tissue. Replacing the X-rays with high energy proton or ion beams poses a solution to this, as protons are able to deposit the majority of their energy in a small region at the tumour site without interacting with the surrounding healthy tissue. This is because heavier particles like protons and ions are able to deposit the maximum energy at the end of their range, whilst lose, undamaging doses are deposited throughout its path [1].

Current X-ray and electron therapy centres have 60% success rate; however, it is estimated that 10-20% of radiotherapy patients would further benefit from access to ion beam therapy [1]. However, accessibility to ion beam therapy is significantly limited and not all patients that would benefit from this treatment are able to receive it. This is due to the current design of the accelerators used to generate these high energy particle beams. These accelerators utilise large and heavy cyclotrons and synchrotrons to generate the particle beam, as well as additional big ion-core magnets and gantries required to transport and deliver such high energy particles [1]. Altogether, this equiptment makes ion-beam therapy non transportable as well as financially demanding, demanding over 100 million Euros to implement [1]. As such, only 89 proton therapy centres exist globally [2].

Laser-driven ion therapy provides a solution to this issue. The heavy and expensive accelerators can be replaced with laser systems to generate and drive the particle beam. Laser-driven systems generate a proton beam by focusing a high-powered pulsed laser onto a specific target. This induces a strong electric field onto the targets surface, which causes the electrons within the material to accelerate away. These electrons generate a strong space-charge field as they leave the surface of the target, which then causes protons and ions at the surface of the target to accelerate away [1]. These accelerated protons form a proton beam that can then be manipulated and transported for treatment. This process is called Target Normal Sheath Acceleration (TNSA). Laser-driven beam facilities are 2-3 times smaller than conventional proton therapy centres, and the simple tabletop lasers required to generate the beam also reduce construction costs [1]. Therefore, the development of laser-driven particle accelerators provides a cost effective and space effective form of ion-beam therapy, allowing treatment to be increasingly available and accessible to those who need it.

1.2 Purpose for Optimising Beamline Energy Delivery

A beamline describes a transport line that contains the source capture and delivery of the laser-driven particle beam. For applications in medicine, the maximum achievable particle flux of laser-driven protons is optimal for effective treatment [3]. Hence it is important to minimise particle losses throughout the beamline in order maximise the delivered flux. Since the particle flux is at its maximum at the source, reducing particle losses in the initial sections of the beamline will significantly maximise the overall delivered particle flux and thus improve the overall efficiency of the beamline. TNSA generated protons are highly divergent as they accelerate away from the laser target [1], therefore strong initial focusing of the beam is required to maximise the number of particles that are accepted within the beamline. By selecting the required particle beam energy as close to the source as possible, the resulting particle flux at this energy can be maximized.

Energy selection of the particle beam can be achieved by variety of different methods. Varying the magnetic fields of pulsed solenoid magnets provides a highly tuneable energy selection method with a large available collection angle to maximise the detected flux [4]. However, these solenoid magnets are significantly more expensive than other focusing magnets. An aperture can also be added to the beamline for energy selection, where its position and aperture can be adjusted to selection specific energy components of the particle beam. However, this energy selection technique requires the beam to be minimally divergent to minimise particle losses at the aperture and maintain a high delivery rate [5].

This report aims to establish an energy selection system within the beamline by varying the quadrupole magnet positions. For each selected energy, the quadrupoles should be in their optimal position such that the overall delivered flux is at its maximum. Energy selection by permanent magnet quadrupoles is effective as it allows for the highly divergent laser-driven particle beam to be simultaneously focused which minimises particle losses caused by divergent particles not reaching the detector. Optimisation by varying quadrupole magnet positions only, and keeping the magnetic strength constant, makes this energy selection method more cost-effective as permanent magnet quadrupoles can be used. A systematic approach will be taken to determine these optimal quadrupole positions so that the physical trajectories through the beamline can be simultaneously studied to explore the relationship between quadrupole position and their focusing effects.

Chapter 2: **Background**

2.1 LION Beamline

2.1.1 Beamline Structure:

This project will optimise the energy delivery for a LION beamline. This specific beamline consists of an initial collimator to collect the generated particles from the source, two permanent magnet quadrupoles (Q1 and Q2) to focus the beam, and a kapton and aluminium foil to capture and collect the focused beam as shown in Figure 1. Quadrupoles magnets have transverse magnetic field lines, so they focus the beamline in transverse directions. Therefore, by combing two quadrupoles, where each quadrupole focuses the beam in each transverse direction respectively, the quadrupole magnets behave as a lens system and a collimated particle beam can be produced [6]. In this LION beamline, Q1 focuses the beam in the x-direction and Q2 focuses the beam in the y-direction. These quadrupole magnets are placed close to the proton source so that they can compensate for the highly divergent nature of TNSA laser-driven protons [7]. The current beamline parametres that define the LION beamline produce a 20.50 MeV particle beam to be delivered at the end of the beamline.
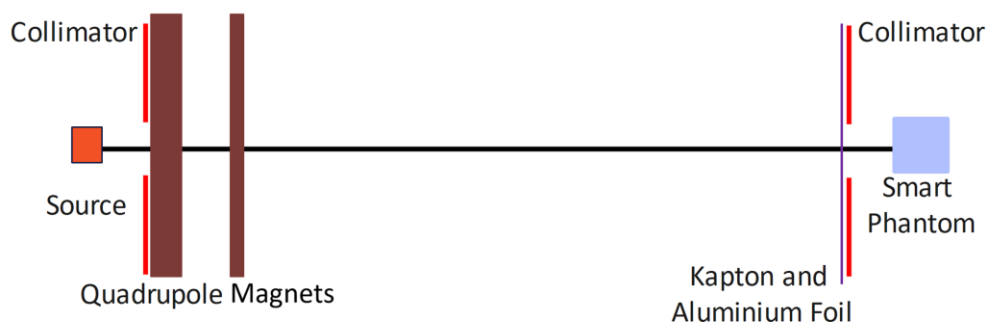

Fig 1. The figure shows a schematic of the composition of the LION beamline. This includes an initial collimator at the particle source, two permanent magnet quadrupoles to focus the beam, and kapton and aluminium foils with a final collimator to capture and collect the beam.

2.1.2 Python Simulation:

A Python simulation was used to model and track particle motion through the LION beamline. The proton source is simulated with the expected TNSA exponentially decaying energy distribution ranging from 1 MeV to 25 MeV. The source is simulated with a symmetric Gaussian shaped beam profile set with a standard deviation of $4x10^{-4}$m. The simulation is characterised by three key object classes. The 'BeamLineElement' class consists of a base class that takes the position and transfer map of a beamline element. Associated derived classes are then defined that specify the transfer map for an aperture, drift space and quadrupole magnets respectively. The 'LIONBeamLine' class reads a given parameter file and uses the 'BeamLineElement' class to arrange the beamline elements in the specific positions that define the LION Beamline. The 'Particle' class is then used to track the 6D trace space of the particles, defined as $(x, x', y, y', z, \delta)$, as they travel through the beamline.

2.2 Particle Motion through Quadrupole Magnets

The magnitude of the magnetic field strength within a quadrupole is directly proportional to the distance from the central axis, where particles travelling far from the central axis experience the greatest focusing effects. The equations of motion for a particle travelling through a quadrupole are deduced with Hamiltonian mechanics. Firstly, the Hamiltonian for a relativistic particle is defined as Eq. 1, where $\mathbf{p}$ is the canonical momentum and $\mathbf{A}$ and φ are the vector and scalar electromagnetic potential [8]. For particle tracking, it is easier to work with the distance along the beamline (Z) as the independent variable of the Hamilton equations instead of time (t). This is because the longitudinal distance travelled by a particle to reach a quadrupole is a fixed value whereas the time taken for a particle to reach this point is known with less accuracy. A conversion between z and t as the independent variable is achieved by replacing t by Z in the Hamiltonian, as well as redefining H as $-p_Z$. Therefore Eq.1 is redefined as the total energy (E) and re-arranged for $-p_Z$ to define the new Hamiltonian as shown in Eq. 2.

$$E = H = c\sqrt{(\mathbf{p} - q\mathbf{A})^2 + m^2c^2} + q\varphi \tag{1}$$

$$H' = -p_Z = \sqrt{\frac{(E-q\varphi)^2}{c^2} - (p_x - A_x q)^2 - (p_y - A_y q)^2 - m^2c^2} - A_z q \tag{2}$$

The longitudinal variables of the Hamiltonian in Eq. 2 are t and $-E$, however for more accurate particle tracking, it is more efficient to work with longitudinal distances. Thus, a canonical transformation is applied to the Hamiltonian to change the longitudinal variables from $t, -E$ to z, δ as shown in Eq. 3. z and δ represent the longitudinal distance and energy of a particle relative to a defined reference particle. For a quadrupole, this reference particle lies on the central z-axis. The resulting Hamiltonian is then scaled for convenience and is shown in Eq. 4. This Hamiltonian can be applied to solve the equations of motion of a particle through any element in a beamline.

$$\delta = \frac{E}{cP_o} - \frac{1}{\beta_0}, \qquad z = \frac{s}{\beta_0} - ct \tag{3}$$

$$H = \sqrt{(\delta + \frac{1}{\beta_0} - \frac{q\varphi}{cP_o})^2 - (p_x - a_x)^2 - (p_y - a_y)^2 - \frac{1}{\beta_0^2 \gamma_0^2}} - a_z \tag{4}$$

To apply Eq. 4 to a quadrupole, the associated scaled vector potential is subbed into the Hamiltonian and a binomial expansion of momentum upto first order terms is applied to produce the final Hamiltonian for a particle in a quadrupole, as shown in Eq. 5, where k_1 is the normalised magnetic field strength. The equations of motion can then be deduced by through Hamilton's equations. The solutions are represented as a linear transfer matrix, as shown in Eq. 6, where L is the quadrupole length and ω is the sqaure root of k_1. Therefore, the 6D phase space vector of the particle, defined as $(x, p_x, y, p_y, z, \delta)$, after travelling through the quadrupole can be determined by matrix multiplication with the particles initial phase space, as used in the Python simulation.

$$H = \frac{p_x^2}{2} + \frac{p_y^2}{2} + \frac{\delta^2}{2\beta_0^2 \gamma_0^2} + \frac{k_1}{2}(x^2 + y^2) \tag{5}$$

$$R_{quad} = \begin{pmatrix} \cos(\omega L) & \frac{\sin(\omega L)}{\omega} & 0 & 0 & 0 & 0 \\ -\omega\sin(\omega L) & \cos(\omega L) & 0 & 0 & 0 & 0 \\ 0 & 0 & \cosh(\omega L) & \frac{\sinh(\omega L)}{\omega} & 0 & 0 \\ 0 & 0 & \omega\sin(\omega L) & \cosh(\omega L) & 0 & 0 \\ 0 & 0 & 0 & 0 & 1 & \frac{1}{\beta_0^2 \gamma_0^2} \\ 0 & 0 & 0 & 0 & 0 & 1 \end{pmatrix} \tag{6}$$

Chapter 3:   **Discussion of Methods Employed**

3.1 Systematic Study of Proton Beam Focusing

3.1.1 Studying Particle Trajectories and Beam RMS

Several preliminary investigations were carried out to develop a thorough understanding of particle motion through the LION beamline. Firstly, the trajectory of delivered particles at each energy was plotted separately to study how each component is focused by the quadrupoles, as shown in Figure 2. These plots show that as the energy of the beam increases, the focal point of the beam occurs at an increasing position along the z-axis. This distribution of focal points can also explain the gaussian shaped delivered energy distribution. The peak delivered energy value is the beam that is focused directly onto the detector plane and the delivery rate decreases as the particles energy deviates from this peak value because the focal point in the beamline becomes further away from this end collimator plane.
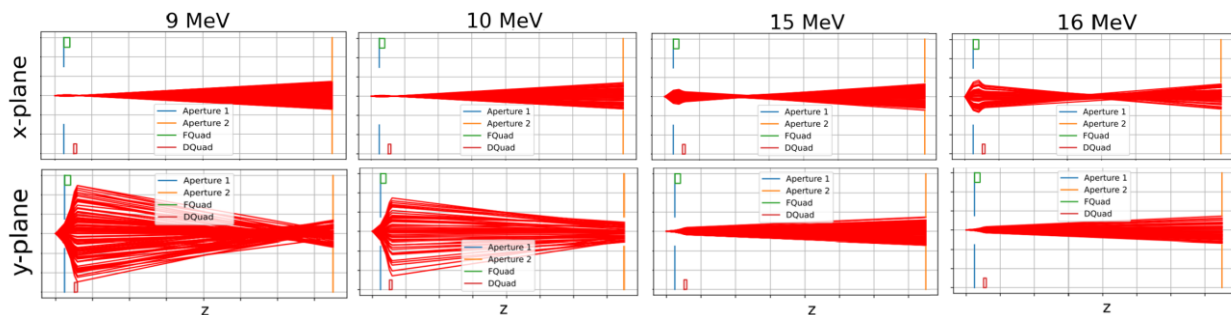

Fig 2. This figure shows the particle trajectory of four energy components of the delivered particle beam: 9 MeV, 10 MeV, 15 MeV and 16 MeV. The top subplots show the trajectory in the x-plane and the bottom subplots shows the trajectory in the y-plane. The trajectories produced a two peak energy histogram at delivery: one peak at 9.25 MeV and the other at 16.75 MeV.

Figure 2 shows that the strength of the quadrupole magnet focusing is the greatest for particles that diverge most from the central axis, as predicted by the previously derived quadrupole magnet transfer matrices. It should also be noted how the focal point of particles at a particular energy occurs at different positions in each transverse plane. This means that a particle beam focused on the end collimator in one transverse plane will significantly diverge at this detection plane in the other transverse plane and the delivered energy will focus in a line. By comparing the focal points in each plane in Figure 2 to the two-peak delivered energy histogram, the 9.25 MeV delivered energy peak seems to arise due to focusing in the y-plane, where the focal point of the 9 MeV beam is shown to focus near the end collimator. And conversely the 16.75 MeV delivered energy peak seems to arise due to focusing in the x-plane.

By re-plotting the particle trajectory with the orignal LION beamline parameters, that produce a single peak energy histogram at 20.50 MeV, the same energy beam was observed to have the same focal point in each transverse direction. The maximum delivery rate is achieved when the focal points in both transverse directions are equivalent because this allows for the maximum number of particles at this energy to pass through the final aperture. Therefore, to optimise the beamline elements so that the delivery rate is maximised, we should aim to adjust the quadrupole positions such that the focal point distribution along the z-axis is equivalent in each transverse direction and the same energy is focussed on the end collimator.

3.1.2 Investigating the effect of Initial Aperture Variations on the Delivered Energy

The aim of this preliminary investigation was to determine if the initial aperture's radius and position should also be varied in the optimisation strategy. Theoretically, increasing the radius of the aperture or decreasing the distance between the source and the initial aperture will increase the accepted solid angle of particles that can enter the beamline, which should maximize the delivered energy rate. The particle trajectories achieved by applying these variations are shown in Figure 3, where altering both the position and radius is shown to increase the divergence of the particle beam through the beamline. However, this does not have a significant impact on the delivered count rate because the delivered particles are restricted by the radius of the final aperture. All the additionally accepted divergent particles are clipped off by this aperture and are not included in the final delivered energy beam. Increasing the reliance on the final aperture to regulate the shape of the delivered beam will cause damage such that it will require frequent replacing. These additional particle losses also can also induce damaging heating effects throughout the beamline [9]. Thus, an efficient beamline would find a comprise between maximising the delivered rate and minimising the damage to the beamline elements. For this optimisation, we decided that the benefit of increased delivery rate was not worth the damage risks within the beamline. Thus, the initial aperture was not included in this optimisation.
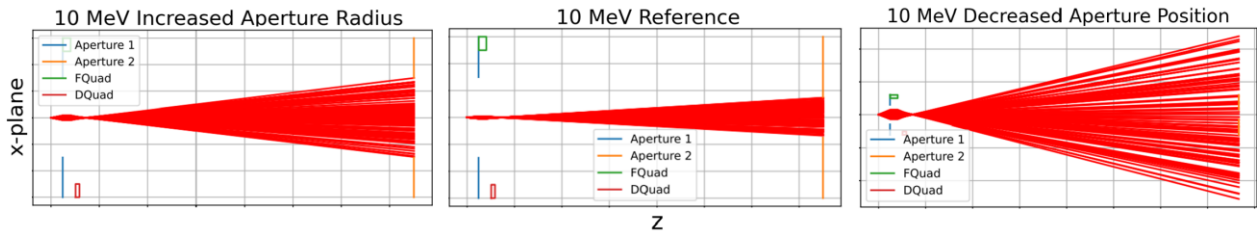

Fig 3. This figure shows how the particle trajectory of 10 MeV particles varies with the initial aperture radius and position. The middle subplot shows the initial trajectory. The first subplot shows the trajectory after increasing the radius of the aperture by 0.0015 m compared to the middle subplot. The last subplot shows the trajectory with the aperture shifted by 0.04m away from the source. The particles that are lost at this end collimator are also plotted to show how this aperture variation produced highly divergent particles that are clipped off at the final aperture.

3.2 Optimisation Method:

The aim of this project was to determine the optimal quadrupole positions to maximise the delivery rate for any specified peak energy. A systematic approach was taken to build an understanding of how this maximum point arises. The current LION beamline parameters that achieve a 20.50 MeV energy peak at delivery are used as a starting point. Starting from this Q1 position, five Q1 positions were chosen at 0.005m intervals. By simulating the beamline with 1000000 particles at the source with a range of Q2 positions for each chosen Q1 position, we aimed to identify five pairs of quadrupole positions that achieve the highest delivery rate at five different energies. Additional simulations where run around the found optimal Q2 value to increase the precision of the optimised results. To study the how the beam focusing varies with quadrupole position, the RMS of the particle beam in each transverse plane was also plotted for each simulation. Therefore, by fitting two separate functions to the variation of optimal Q1 and Q2 positions against their associated delivered energy, two conversion functions can be derived that will take any desired energy delivery as an input and calculate the optimal quadrupole positions required to achieve this. To implement this method with the given Python simulation, the input parameter file was used to vary the quadrupole arrangement within the beamline. The length of the initial drift space and the drift space between quadrupoles was varied to change the quadrupole positions, and the main drift length was subsequently adjusted so that the final collimator position remained fixed for each simulation.

Chapter 4:   **Results and Discussion**

4.1 Varying Second Quadrupole Position

4.1.1 Delivered Energy Spectrum

The following results show how the delivery energy spectrum varies with the second quadrupole position. For the data found in Figure 4, the first quadrupole position was fixed at 0.04034m. At the lowest quadrupole seperation of 0.01577m, two peaks can be seen in the delivered energy histogram. As the distance between quadrupoles increases, the distance between these peaks seems to decrease. When these peaks merge, the number of particles reaching the end collimator increases significantly, reaching upto 4000. This delivery rate is a maximum when the distance between quadrupoles is 0.03177m, with a peak delivered energy of 10.25 MeV. Therefore, we can conclude that Q1 at 0.04034m and Q2 at 0.03177m from Q1 give the optimised parameters to deliver a 10.25 MeV proton beam. Furthermore, as the seperation distance between the quadrupoles increases, the energy of one peak seems relatively constant around 10 MeV whereas the energy of the second peak seems to be significantly increasing. This suggests the second quadrupole position primarily effects how particles at this second peak focus at the end collimator.
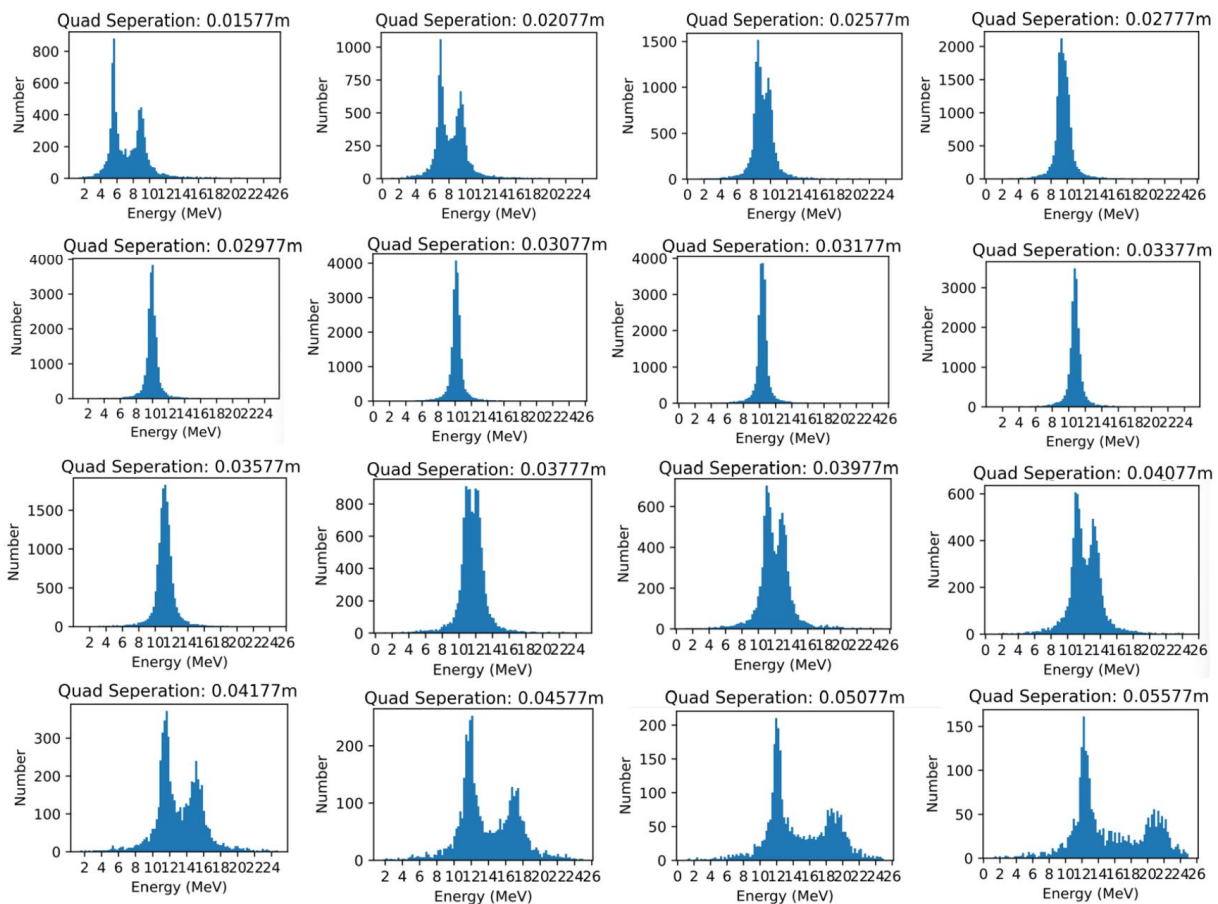

Fig 4. These plots show the delivered energy histogram for each second quadrupole position. The first quadrupole was fixed at 0.04034m. Each histogram represents the energy delivery at an increasing Q2 position, with the Q1 position fixed. The energy histogram is seen is approach a maximum rate when the second quadrupole is at 0.03377m.

4.1.2 RMS of the Proton Beam across Beamline

The RMS of each energy component of the beam shows the how the quadrupole positions affect the focal points for each particle energy. Figure 5 shows the RMS in each transverse plane for a two-peak delivered energy histogram; one peak was centred at 8.75 MeV and the other peak at 13.75 MeV. In the initial section of the beamline, the 14 MeV particles are the most divergent in the x-plane and the 9 MeV particles are the most divergent in the in the y-plane. This is seen as the RMS at these energies rapidly increases as the travel away from the source. These beams reach the closest transverse distance to the quadrupole magnets, so they experience the strongest magnetic field and become the most focused energy component in the beamline. This is seen Figure 5, as these energy components become the most re-focused and reach the end of the beamline with the lowest non-divergent RMS in each plane. This means that these energies are delivered with minimal clipping at the final aperture and define the peaks in the delivered energy histogram.
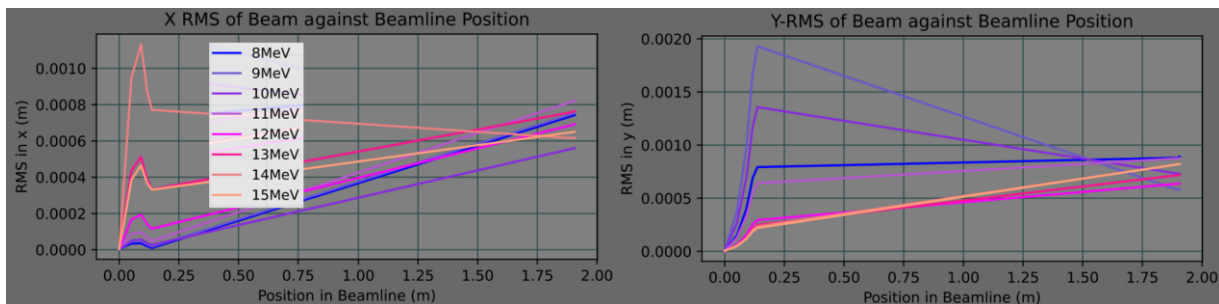

Fig. 5. The plots show the RMS of each energy component of the particle beam as it travels through the beamline. The Q1 was simulated at 0.05034m and the seperation between quadrupoles at 0.03577m. The delivered energy histogram shows one peak is centred at 8.75 MeV and another peak at 13.75 MeV.

Figure 5 and Figure 6 show the RMS of the particle beam where the first quadrupole is in the same position, but the second quadrupole is shifted by 0.01m. The most focused energy component changes from 14 MeV to 16 MeV in the x-plane, and from 9 MeV to 16 MeV in the y-plane. This suggest that shifting the second quadrupole has a greater effect on the energy focused in the y-plane. This supports the conclusion made from the trend observed from the delivered energy histograms in Figure 4. Shifting the second quadrupole position primarily controls the energy focused in the y-plane, which defines the energy of the secondary peak in the delivered energy distribution. The energy delivered in the x-plane still shifts slightly due to the nature of the magnetic field within a quadrupole. Whilst a quadrupole induces focusing in one transverse direction, a smaller defocusing effect is induced in the other transverse plane. Therefore, the energy focused in each transverse pane is shifted, which is why the primary peak in Figure 4 was seen to shift slightly with Q2 position. However, this effect in one transverse direction is much greater than the other. Figure 6 shows the same 16 MeV beam as the most focused component in each transverse plane, which resulted in the single peaked energy histogram.
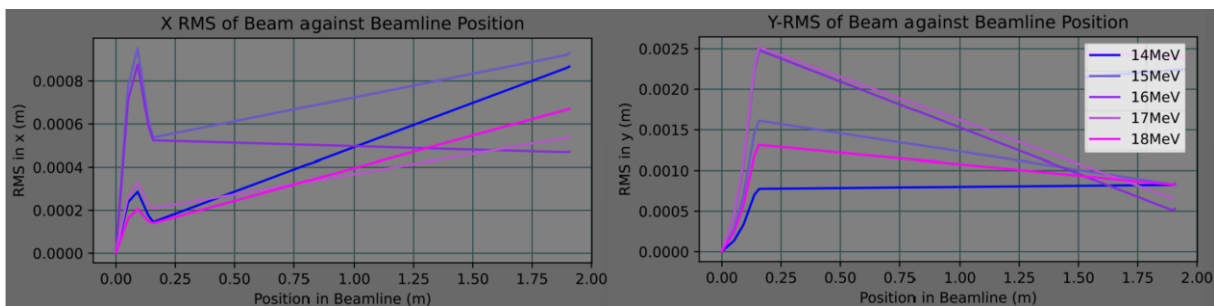

Fig 6. These plots show the RMS of each energy component of the particle beam as it travels through the beamline. The Q1 was simulated at 0.05034m and the seperation between quadrupoles at 0.04577m. The corresponding delivered energy spectrum was a single peaked histogram centred 15.75 MeV.

4.2 Results at all First Quadrupole Positions

4.2.1 Delivered Energy Spectrum

The above data collection process was repeated for four different Q1 positions. The resulting delivered peak energy values are shown in Figure 7. The errors associated with the delivered energy values were calculated by combining the error in fitting a gaussian function to the delivered energy spectrum, as well as ± 0.125 MeV from the bin width in the energy histogram. Since a symmetrical gaussian shaped delivered energy peak is the desired energy distribution of the particle beam for further applications, this fitting error seems to be a valid way to measure any asymmetries and irregularities in the delivered energy distribution.
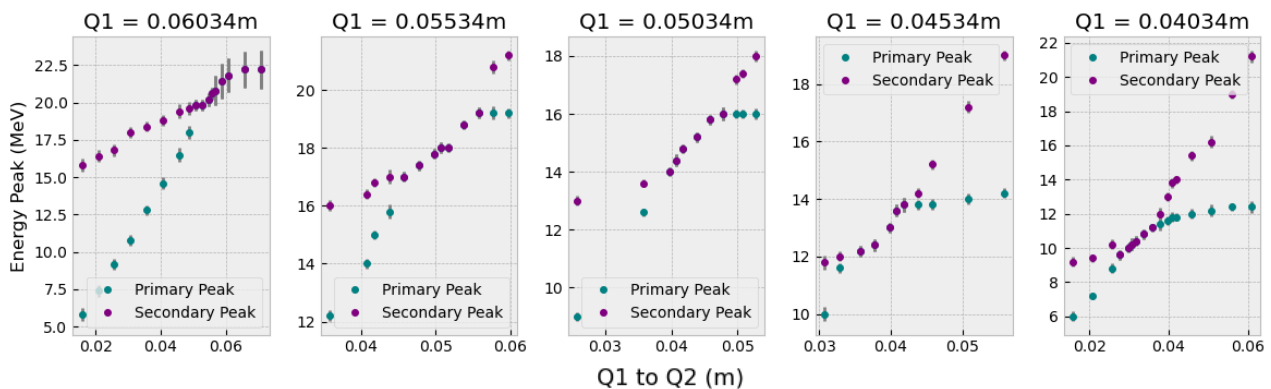

Fig 7. This figure shows the peak delivered energy across different quadrupole separation distances. Each subplot represents a different first quadrupole position. The 'Primary Peak' represents the energy peak with the highest rate at delivery and the 'Secondary Peak' represents the peak with the lower delivery rate.

Overall, the energy of the delivered beam increases as the quadrupole seperation distance increases. The plots show that for a finite range of quadrupole seperation values, the primary and secondary peak data points merge, which represents a single peak in the delivered energy distribution. Figure 7 shows that the energy of the primary peak is always less than the energy of the secondary peak. This is due to the exponentially decaying nature of the energy distribution at the source, which means that a higher number of low energy protons are emitted into the beamline. Thus, the delivered energy peak at lower energies will have a greater delivery rate than that of higher energies.

4.2.2 Variation of Delivered Rate with Quadrupole Positions

In order to determine the optimal quadrupole positions that maximize the delivered particle flux, the relationship between particle delivery rate and quadrupole positions was also investigated. Figure 8 shows how the number of particles at the peak energy at delivery varies with quadrupole separation distance. The errors in particle number are determined by the gaussian fitting errors. The maximum delivery rate is achieved for lower energies and seems to exponentially decrease due to the exponentially decaying energy distribution at the source. Moreover, each Q1 position, labelled separately in Figure 8, appears to have a distinct energy value where a maximum delivery rate is reached. This shows that, for each Q1 position, there exists a unique and distinct Q2 position such that a maximum delivery rate is achieved. This is the Q2 position that was taken as the optimised position result.
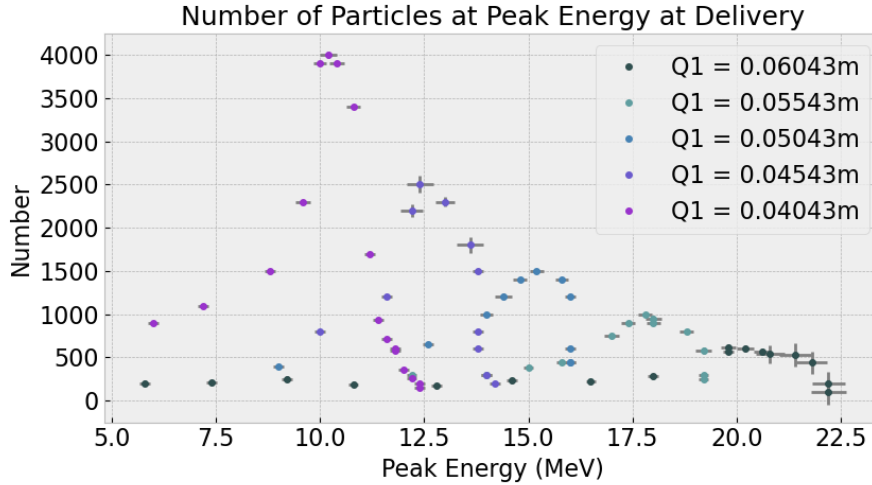
Fig 8. This graph shows the total number of particles at the peak energy in the delivered energy spectrum against the associated peak energy value. The five different simulated Q1 positions are labelled respectively.

4.3 Overall Optimised Quadrupole Position Results

Using the above collected data, five distinct sets of Q1 and Q2 positions that have been proven to optimise the energy delivery rate can be determined. Figure 9 shows all five optimised parameters, where each optimised quadrupole position is plotted against its associated optimised delivered energy. The quadrupole position errors were calculated as the distance between each simulated quadrupole position data point. The Q1 positions seem to follow a strong linear correlation with the delivered energy and the Q2 positions from Q1 seem to follow a higher order polynomial correlation with energy. Therefore, by fitting the Q1 position results to a linear function and the Q2 from Q1 distance results to a quartic function, a set of functions can be derived to convert the desired delivered energy into the optimal quadrupole positions required to achieve this. These functions are shown in Eq. 7 and Eq. 8.

A quartic function was chosen to fit the data against because higher order terms in the polynomial will allow for smaller adjustments in the function to increase the accuracy of the fit to the data. However, by comparing the order and magnitude of each term and the fitting errors for different polynomial fits, the cubic and quartic term appeared to be negligible to the overall accuracy of the fit, so are not included in the below function.

$$Q_1(E) = (0.211E + 2.008) \times 10^{-2} \tag{7}$$

$$Q_{2\,from\,1}(E) = (-0.008E^2 + 4.139E - 3.637) \times 10^{-3} \tag{8}$$
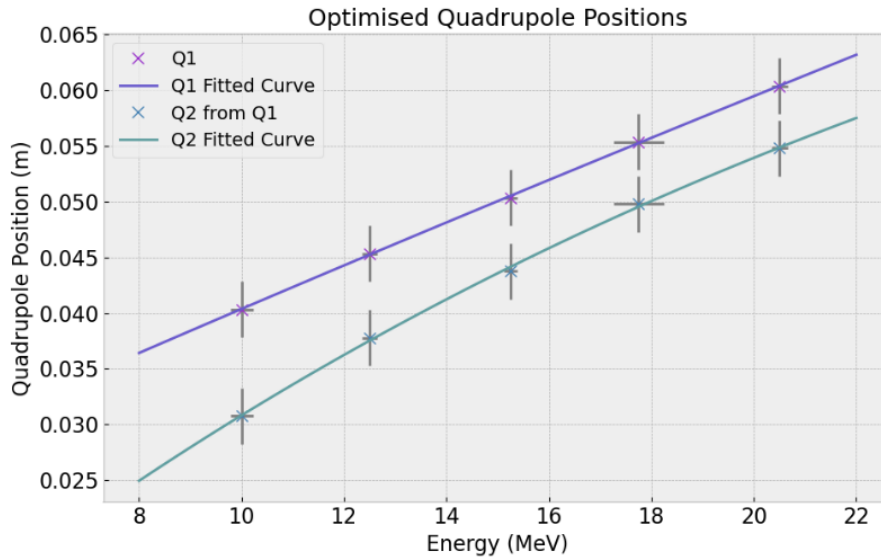
Fig 9. This graph shows the optimised quadrupole positions against the peak energy that they optimise for at delivery. The equations for the fitted curves are presented in Eq. 7 and Eq. 8 and are used to calculate the optimal quadrupole positions for any desired peak energy at delivery.

To verify that these fitted functions can calculate accurate quadrupole positions that will optimise the beamline, they were used to optimise the beamline for a 14MeV energy peak at delivery. The simulation was run with the optimised quadrupole position given by Eq. 7 and Eq. 8 and the resulting energy histogram is shown in Figure 10. This figure shows a peak delivered energy at 14 MeV, where the achieved rate aligns with the expected maximum achievable rate from Figure 8. This verifies the accuracy of Eq. 7 and Eq. 8 to calculate the quadrupole positions required to achieve any desired peak energy at delivery at a maximum rate.
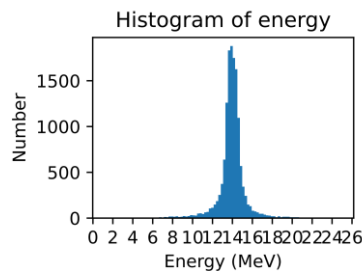

Fig 10. This figure shows the delivered energy histogram achieved by setting the quadrupole positions as defined in Eq. 7 and Eq. 8 to achieve at 14 MeV peak at delivery. The deduced optimised Q1 position was 0.04812m and the Q2 from Q1 distance was 0.04123m.

Chapter 5:   **Supplementary Results and Discussion**

5.1 Exploring the Relationship between Quadrupole Position and Delivered Energy

From the transfer matrix for quadrupole magnets derived in Chapter 2, we can see that the particle trajectory across a quadrupole magnet is dependent on three parametres: the quadrupole length L, the normalised quadrupole magnetic field strength k_1 and the particles initial trace space vector. The trace space vector is defined as $(x, p_x, y, p_y, z, \delta)$, where x' and y' represent the derivative of x and y with respect to z. This vector is used in the simulation to propagate the particle beams. Since L and k_1 are fixed, the initial trace space vector must be the parameter that distinguishes the particle trajectory of each energy particle beam. This is determined by the initial trace space of laser driven TNSA protons that is modelled in the simulation. To investigate this, the x' and y' of protons from the trace space at the source was plotted against the particle energy. Within the small angle approximation, these quantities represent the angle of emittance of the particle from the source in each transverse plane [10]. Figure 11 shows this source distribution, where x' and y' seem to follow an exponential relationship with particle energy.
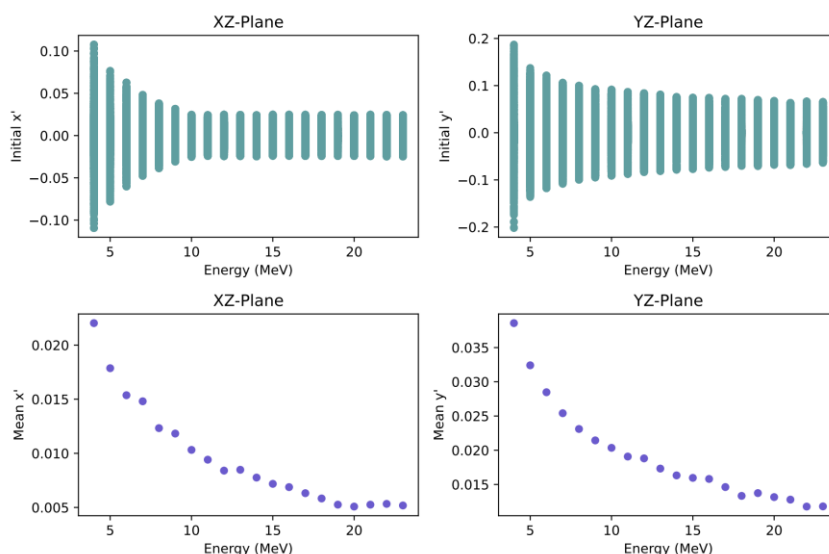

Fig 11. Initial x' and y' of particles as a function of particle energy. The top row plots represent the x' and y' value per particle and the bottom row represents the overall mean value at each energy. An exponential relationship between particle energy and x' or y', which represents the emittance angle in each transverse plane, is observed.

This shows that the emittance angle of particles at the source have an energy dependence. At the source, low energy protons are the most divergent component of the particle beam. As the energy of the beam decreases, the emittance angle decreases and the overall divergence of the beam at this energy decreases. This is a result of how the TNSA laser-driven protons are produced, where the electrons that are initially accelerated away from the target material from a gaussian shape in the transverse plane. This electron sheath then induces the emitted protons to have curved opening angles [10].

These results show that as the energy of the particle decreases, the particles reach Q1 with increasing divergence. Depending on the position of Q1, significantly divergent protons will be clipped off by the aperture of the quadrupole. Since the low energy particles are the most divergent component of the beam, they will be the first component to be clipped off the quadrupole aperture. As the distance between the source and Q1 increases, the divergence of particles will increase so more particles are clipped off. Therefore, the particles in the beam will be clipped off in order of decreasing energy. From this we can conclude that as the distance between the source and Q1 increases, the energy of the accepted protons will increase therefore the energy of the overall delivered proton beam will increase. This explains the trend observed Figure 7 and Figure 8, where the peak delivered energy increases with quadrupole position.

5.2 BDSIM Simulation Comparison

5.2.1 BDSIM Simulations

Beam Delivery Simulation (BDSIM) is a Geant4 based program used to simulate the passage of particles through a particle accelerator [9]. While the python simulation used in this report uses linear transfer maps to track the particle through the beamline, BDSIM also takes into acount the interactions between particles and the materials of the accelerator. The inclusion of this interaction is crucial for accurate particle tracking. When divergent particles impact the edges of the particle accelerator, large amounts of radiation is produced which can contribute to damaging heat loads or generate additional background radiation that can reach the detector. These particles can also scatter and re-enter the detected particle beam, therefore will contribute to the overall delivered energy histogram [9]. Therefore, BDSIM models provide a more accurate representation of the delivered energy distribution than the python simulation used here. To investigate the effect of particle-matter interactions on the deduced optimised results, two sets of the optimised quadrupole positions were ran using the BDSIM model. The resulting delivered energy histogram from each model was compared to explore the impact of particle-matter interactions on the overall delivered energy.

5.2.2 Comparing the BDSIM and Python Energy Delivery Histograms

The optimised quadrupole positions to produce a 10.25 MeV and 15.25 MeV energy peak at delivery were each simulated respectively. The energy distribution from each simulation is presented in Figure 12. Both simulations show agreement with the position of the peak in the delivered energy spectrum. This peak energy value is equivalent in both simulations for the second set of test parametres, however it deviates by 0.50 MeV for the first test parametres. The peak energy value is limited by the 0.5 MeV bin width of the energy histogram in the BDSIM model, which makes it difficult to determine whether this deviation in peak energy is a consequence of particle-matter interactions. Hence a 0.50 MeV deviation in peak delivered energy is small enough to conclude that the BDISM results support the optimised results achieved in this report.
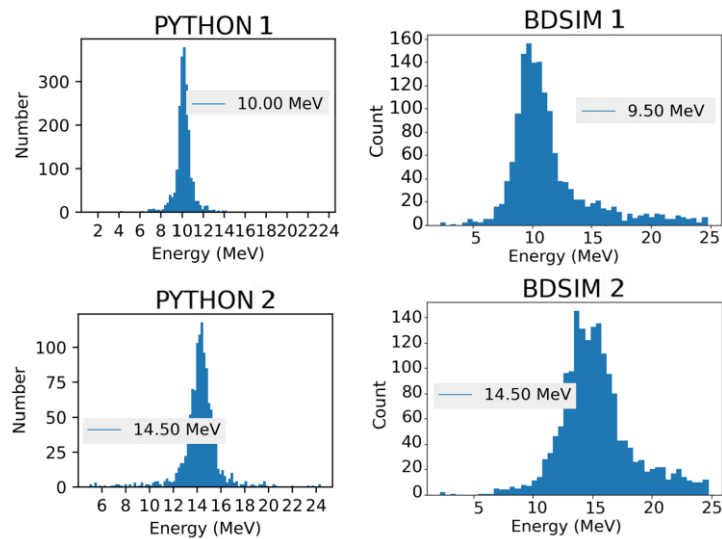
Fig 12. This figure shows the delivered energy histograms achieved from a python simulation and a BDSIM simulation with two different sets of optimal quadrupoles positions. These plots show that the optimised quadrupole positions produce a delivered energy spectrum with the same peak energy value in each model. The energy histograms on the top row were simulated with Q1 at 0.04043m and the distance between quadrupoles as 0.03077m. The plots on the bottom row were simulated with Q1 at 0.05043m and the distance between quadrupoles as 0.04377m.

Although these simulations show agreement with the peak delivered energy value, the energy histogram produced by the BDSIM simulation shows a broader range of energies reaching the end collimator. This effect could be a consequence of particle-matter interactions, where particles at a range of energies are reflected at the beamline boundary and reach the end collimator. However, whilst studying this simulation, it was noticed that each simulation was run with a different energy distribution at the source: the python simulation was run with an exponential energy distribution whereas the BDSIM simulation was run with a uniform energy distribution. Hence a higher number of particles at higher energies are simulated at the source in the BDSIM model which causes a higher number of particles at these energies to reach the detector. To improve the validity of this comparison, the Python simulation should be re-run with a source with a uniform energy distribution.

Chapter 6:   **Conclusion**

6.1 Areas for Improvement

A limitation with the energy selection method described here is that precisely adjusting the quadrupole positions is difficult to practically implement. To change the energy delivered by 1 MeV, the quadrupoles need to be shifted by just a few millimetres, which is difficult to achieve accurately with big heavy permanent magnet quadrupoles.

It would have been interesting to explore an energy selection method by using an additional aperture. In this project, it was found that a two-peak delivered energy histogram was the result of different energies being focused at the end collimator in each transverse direction. Therefore, by placing an elliptical aperture in the beamline, where the radius is very narrow in one transverse direction, the energy focused in one transverse plane could be theoretically clipped off and the resulting energy histogram would just have one peak from the non-clipped component of the beam. Although the delivery rate of this energy would be significantly lower than the rate achieved by quadrupole position manipulation, an adjustable aperture could provide an alternative energy selection method that is more easily implementable.

The RMS model of the beam throughout the beamline could also be improved. The RMS was calculated as the average RMS of all particles in the beam. However, this may not be an accurate representation of the RMS of the enitre beam at this energy. This calculation may include the RMS of stray, highly divergent particles that do not fully represent the average RMS of the entire beam. To improve this model, the distribution of the RMS of each particle at each energy in the beamline could be plotted at each section in the beamline. From this distribution, only the RMS values with the highest number of particles should be included in the average RMS calculation. This ensures that the calculated RMS value is fully accurate to the distribution of the beam.

6.2 Summary

Overall, two functions were derived that can calculate the optimal quadruple magnet positions required to achieve a specific energy peak at delivery. These quadrupole positions will achieve the maximum delivery rate of particles at this energy. The quadrupole position given by these functions were tested to produce an arbitrary 14 MeV peak energy, which verifies the validity of these results. The particle trajectories and RMS variations through the beamline where also studied to observe how the particle beam at each energy is focused throughout the beamline and how these focussing effects change as the quadrupole positions shift. It was concluded that, to achieve a maximum delivery rate, the focal point of the particles at the desired energy should occur at the plane of the detector. Due to the transverse nature of quadrupole magnet focusing, each energy component may have a different focal point in each transverse plane. Therefore, an optimal set quadrupole positions will focus the same energy at the detector in each transverse plane to minimize particle losses by clipping at the final aperture and maximise the delivery rate. The optimal quadrupole parameters where also tested with a BDSIM simulation, which provides a more accurate model for particle motion within a beamline. Although discrepancies in energy distribution width where observed, the position of the peak energy from the BDSIM model agrees with the python simulation results. This supports the relationship between peak delivered energy and quadrupole position that has been derived in this report.

Bibliography

[1] Masood, U., Bußmann, M., Cowan, T.E., W. Enghardt, Karsch, L., Kroll, F., Schramm, U. and Jörg Pawelke (2014). A compact solution for ion beam therapy with laser accelerated protons. Applied Physics B, 117(1), pp.41–52. doi:https://doi.org/10.1007/s00340-014-5796-z.

[2] Munzenrider J. E.; Liebsch N. J. (1999). Proton radiotherapy for tumors of the skull base. Strahlenther. Onkol. 175: 57–63. doi:10.1007/bf03038890

[3] Sciscìò, M., Migliorati, M., Palumbo, L. and Antici, P. (2018). Design and optimization of a compact laser-driven proton beamline. Scientific Reports, 8(1). doi:https://doi.org/10.1038/s41598-018-24391-2.

[4] Wu, M., Zhu, J., Li, D., Yang, T., Liao, Q., Geng, Y., Xu, X., Li, C., Shou, Y., Zhao, Y., Lu, Y., Lu, H., Ma, W., Lin, C., Zhu, K. and Yan, X. (2020). Collection and focusing of laser accelerated proton beam by an electromagnetic quadrupole triplet lens. Nuclear Instruments and Methods in Physics Research Section A: Accelerators, Spectrometers, Detectors and Associated Equipment, 955, pp.163249–163249. doi:https://doi.org/10.1016/j.nima.2019.163249.

[5] Scuderi, V., Sayyed Bijan Jia, Carpinelli, M., Cirrone, G.A.P., Cuttone, G., Korn, G., Licciardello, T., Maggiore, M., D. Margarone, Pisciotta, P., Romano, F., Schillaci, F., Stancampiano, C. and Tramontana, A. (2014). Development of an energy selector system for laser-driven proton beam applications. Nuclear Instruments and Methods in Physics Research Section A: Accelerators, Spectrometers, Detectors and Associated Equipment, 740, pp.87–93. doi:https://doi.org/10.1016/j.nima.2013.10.037

[6] Eichner, T., Grüner, F., Becker, S., Fuchs, M., Habs, D., Weingartner, R., Schramm, U., Backe, H., Kunz, P. and Lauth, W. (2007). Miniature magnetic devices for laser-based, table-top free-electron lasers. Physical Review Special Topics - Accelerators and Beams, 10(8). doi:https://doi.org/10.1103/physrevstab.10.082401.

[7] Ter-Avetisyan, S., Schnürer, M., Polster, R., Nickles, P.V. and Sandner, W. (2008). First demonstration of collimation and monochromatisation of a laser accelerated proton burst. Laser and Particle Beams, 26(4), pp.637–642. doi:https://doi.org/10.1017/s0263034608000712.

[8] Appleby, R.B. (2015). Beam Dynamics in High Energy Particle Accelerators, by Andrzej Wolski. Contemporary Physics, 56(2), pp.242–243. doi:https://doi.org/10.1080/00107514.2014.999708.

[9] Nevay, L., Boogert, S., J. Snuverink, Abramov, A., Deacon, L., H. García Morales, Lefebvre, H., Gibson, S.M., Kwee-Hinzmann, R., Shields, W. and Walker, S.D. (2020). BDSIM: An accelerator tracking code with particle–matter interactions. Computer Physics Communications, 252, pp.107200–107200. doi:https://doi.org/10.1016/j.cpc.2020.107200.

[10] Roth, M. and Schollmeier, M. (n.d.). Ion Acceleration-Target Normal Sheath Acceleration *. [online] doi:https://doi.org/10.5170/CERN-2016-001.231.